

ARTICLE OPEN



Probing top-of-the-line corrosion using coupled multi-electrode array in conjunction with local electrochemical measurement

Mingyu Wang¹, Mike Yongjun Tan², Yesen Zhu^{3,4}, Yi Huang ^{1,4} and Yunze Xu ^{1,4}✉

An experimental method has been developed for probing top-of-the-line corrosion (TLC) of pipeline steel based on the use of the wire beam electrode (WBE) in conjunction with local electrochemical measurements. Results show that the location of the droplet, the droplet retention time, the water condensation rate and the local TLC rate could be well determined through the macro-cell current mapping and local electrochemical measurements. The precipitation and the scaling tendency of the FeCO₃ beneath the droplet were quantitatively estimated. The micro-cell corrosion was significantly influenced by the thickness of the condensed water film and the protectiveness of the FeCO₃ layer. The discrepancy of the film formation inside and outside the droplets was the driving force of macro-cell corrosion. The in-situ measurement and visualization of the corrosion processes and kinetics using the modified WBE could be conveniently used to facilitate the understanding of the initiation and propagation of localized TLC.

npj Materials Degradation (2023)7:16; <https://doi.org/10.1038/s41529-023-00332-x>

INTRODUCTION

Top-of-the-line corrosion (TLC) is a challenging and unsolved issue that affects many crude oil and gas transportation pipelines where major temperature differences exist between the transported medium and the pipe outer environment^{1–7}. When the temperature of the internal pipe wall is lower than the water dew point, water in the hot gas and vapour would condense and form droplets on the top of the pipe wall. The condensed water could become corrosive with the dissolution of carbon dioxide (CO₂), hydrogen sulphide (H₂S), volatile organic acids and sometimes oxygen in it^{8–10}, causing TLC. TLC is known to be affected by many factors including water condensation rate, water chemistry, partial pressure of acidic gases (e.g. CO₂ and H₂S), gas flow rate, the presence of organic acids (e.g. HAc), the formation of protective scales, and the presence of sulphate-reducing bacteria^{3,5,11}. TLC could not be controlled by corrosion inhibitors, the most efficient methods of pipeline corrosion mitigation, because traditional non-volatile corrosion inhibitors that are commonly added in the liquid phase in flowlines for corrosion control could not reach the top of the pipe at the stratified flow regime, and therefore TLC remains a major threat for the integrity of oil and gas pipelines^{12,13}.

Major efforts have been made to develop corrosion inhibitors that could reach the top of the pipe^{12,14–16}. One approach is to develop volatile corrosion inhibitors that are able to reach the condensed water at the top of the line, making corrosion inhibition useful for TLC prevention. Unfortunately, the discovery and evaluation of such volatile corrosion inhibitors is not an easy task because of technological difficulties in measuring, monitoring and evaluating the effects of such inhibitors in the condensed water droplet at the top of the pipeline. TLC is an ‘invisible’ and dynamically changing localised corrosion that occurs on pipe internal surface, currently there is a lack of effective techniques that could be used to perform in-situ probing and monitoring of TLC.

The gravimetric measurement using weight loss coupons is the most common method in TLC studies^{17–19}. The general corrosion rates could be obtained from the mass difference of the coupon before and after a period of TLC. Meanwhile, the change of the surface morphologies could be characterized visually and microscopically to further understand the localized corrosion behaviour beneath the condensed water droplet. However, weight loss coupons are not easy to be installed on and withdrawn from the internal surface of practical oil and gas pipelines and frequent shut down of the operation system would be needed for coupon installation and collection^{20–22}. The dynamic change of the corrosion rates caused by the droplet renewal, corrosion inhibitors and the environmental variation could not be detected by the periodical weight loss measurement. In order to overcome the difficulty in on-line monitoring of TLC, electrical resistance (ER) probes which is also called ‘intelligent coupon’ are adopted to provide continuous measurement of TLC^{14,21,22}. The wall thickness reduction of the ER probe could be captured from the resistance increasing of the ER probe. However, the temperature fluctuation has a dramatic interference on the ER measurement and would lead to measurement errors in ER probe measurement^{23,24}. Another limitation of the ER method is that the resolution of the sensor is determined by the thickness of the sensing element. It may take several weeks to respond to the corrosion depth of a few micrometres when the thickness of the sensing element is close to the real pipe wall. Thinning of the sensing element could effectively promote the resolution of the ER sensor, while, the reduction of the wall thickness would shorten the service life of the probe.

Since TLC is a process of electrochemical reaction, researchers attempted to use electrochemical techniques such as linear polarization resistance (LPR) and electrochemical impedance spectroscopy (EIS) measurements in TLC studies^{16,20,25,26}. In comparison with ER technique, electrochemical methods could

¹School of Naval Architecture and Ocean Engineering, Dalian University of Technology, Dalian 116024, China. ²Institute for Frontier Materials, Deakin University, Waurn Ponds 3216 VIC, Australia. ³PowerChina Huadong Engineering Corporation Limited, Hangzhou 311122, China. ⁴State Key Laboratory of Structural Analysis, Optimization and CAE Software for Industrial Equipment, Dalian University of Technology, Dalian 116024, China. ✉email: xuyunze123@163.com

provide an instant response to the corrosion processes, suggesting that the dynamic changes of the corrosion status could be immediately detected without a long delay. However, in practical TLC applications using traditional three or two electrodes system, the low conductivity and the thin film of the condensed water would lead to a high solution resistance between the working electrode (WE) and the counter electrode (CE), which significantly limits the application of LPR and EIS probes using a small potential or current stimulation^{22,27}. A modified method using the collected condensed water of dozens of millilitres for electrochemical measurements is performed in some TLC studies. The collected condensed water could restore the original corrosive environment beneath the water droplet in some extent, however, the mass transfer process, the distribution of the condensed water and the chemical and electrochemical heterogeneity beneath the droplet are totally different from those in the collected condensed water. Therefore, the real TLC behaviour could not be accurately revealed using this approach. Recently, mini-electrodes with the diameters of a few millimetres is introduced into the TLC studies to perform the localized electrochemical measurements²⁵. The tiny electrodes could significantly reduce the measurement error induced by the high solution resistance in the water droplet, however, the tiny electrodes could only be placed in a certain part of the water droplet due to the limitation of the electrode dimension and therefore the general TLC behaviour is hard to be measured using only a set of mini-electrode three electrodes system. Additionally, it is known that the distribution of the water droplets on the steel is random and the droplets are normally separated from each other. Since the location of the randomly distributed droplets in the pipe could not be visualized, the electrochemical measurement results would dramatically deviate from the real conditions once the tiny electrodes are rightly placed in certain droplets.

Although various efforts were made in past decades to measure and understand the TLC, there is still a lack of effective methods that could accurately sense the dynamic progression of TLC. There is a need for technologies that are effective for volatile corrosion inhibitor discovery and assessment, as well as for the early warning and protection of TLC in energy pipelines^{16,28,29}. In this work, a method which combined the integrated multi-electrode array technique and local electrochemical measurements is proposed for this purpose, and is demonstrated in a typical experiment to visualize and understand the initiation and propagation of TLC in simulated condensed water droplets at the top of pipeline. A 10×10 coupled multi-electrode array, which is also referred to as wire beam electrode (WBE)^{30–36} is employed to detect the distribution of the water droplet on the steel surface through mapping current distributions. Besides, two important parameters of TLC, i.e. the droplet retention time (DRT) and the water condensation rate (WCR) could be measured from the specially designed circuit. After mapping the droplet distribution, the local LPR measurements were performed to investigate localized corrosion beneath the droplet. On the basis of this method and the 3D profile characterization, the contributions of both macro-cell current and micro-cell current on TLC are distinguished and discussed, aiming to address the key parameters which should be concerned in TLC studies.

RESULTS

The measurement results of macro-cell currents on WBE

The formation process of the droplets on the steel surface was photographed by the endoscope (Fig. 1). Liquid embryos started to nucleate on the WBE surface after 0.1 h of test. The tiny droplets gradually formed on the wire electrodes and began to coalesce with each other after 0.5 h of test. The liquid film was firstly observed at the top right corner of the WBE. Along with the continuous condensation of the vapour and the coalescence of

the initial tiny droplets, the thickness of the liquid film kept increasing from 1 h to 2 h, and gradually cover the whole WBE at 2 h. Thereafter, several big droplets evolved on the WBE due to the surface tension. The distribution of the big droplets could be clearly seen at 6 h. A complete droplet which rightly generated at the centre of the WBE is defined as the 'main droplet' in this work. The four corners and edges of the WBE were partially covered by several droplets which main bodies generated on the epoxy resin. A thin liquid film is seen between the boundaries of the water droplets. The locations and the diameters of the droplets kept relatively stable in the following test periods (6–168 h). The diameter of the main droplet reached 12.5 mm which almost covered 50% of the WBE surface. Due to the accumulation of corrosion products around the main droplet, the partial droplets at the corners and edges of the WBE could not be clearly identified from the photos of 168 h. However, these droplets were still observed after the WBE was immediately taken out of the test cell which is similar to the distribution of the water droplets observed at 6 h.

The dynamic change of the macro-cell current map is plotted in Fig. 2. More details of the current mapping at different test duration is plotted in Supplementary Fig. 1. The macro-cell current was tiny at the beginning of the test due to the disconnection of the nucleated tiny droplets at 0.1 h of test. Obvious anodic sites and cathodic sites are observed at the top right corner at 0.5 h which was induced by the formation of condensation film at the local area. The anodes and cathodes became more significant along with the coalescence of the tiny droplets and the thickening of the condensation film (1–2 h). Along with the formation of the stable droplets at 3–6 h, the distribution of the major anodes and cathodes gradually became stable. Most of the wire electrodes beneath the water droplets acted as anodes. While, the major cathodes were distributed beneath the thin condensation film where was outside the droplets. The separation of the major anodes and cathodes became more significant along with the TLC propagation. The boundary of the main droplet could be clearly identified from the distribution of the anodes and cathodes after 48 h of test. Although the boundaries of the droplets at the corners and edges of WBE are hard to be directly seen from the photos at 168 h due to the visual influences of the corrosion products, the local areas beneath the droplets could be well identified from the current map where anodic currents are registered. The current distribution maps also show that the major cathodes and anodes were almost kept unchanged from 72 h to 168 h. These typical anodes and cathodes were all distributed around the boundary of the main droplet.

In order to investigate the influence of the growth and fall of the droplet on the local macro-cell currents, the current distribution maps at three different moments (immediately after droplet falling, droplet growing and right before droplet falling) of a DRT cycle were probed and presented in Supplementary Fig. 2. Both the distribution of anodes and cathodes and the magnitude of the anodic currents and cathodic currents were almost the same over the three different periods, indicating that the fall and retention of the droplet nearly had no influence on the macro-cell corrosion. Two wire electrodes which were located right beneath the droplet ($W_{7,7}$) and beneath the liquid film outside the droplet ($W_{8,10}$) were selected to monitor the dynamic change of the local macro-cell currents for 8000 s. The measurement results are presented in Fig. 3. A sharp change of the macro-cell current would occur after the fall of the droplet. While, the current would soon restore to the original level in a few seconds, also indicating that the fall of droplets only has a slight influence on the corrosion process.

Current spikes were triggered on both the wire electrodes inside and outside the droplet during the droplet falling (Fig. 3). The current spikes were induced by the modification of the double layer on the steel interface. The DRT could be obtained

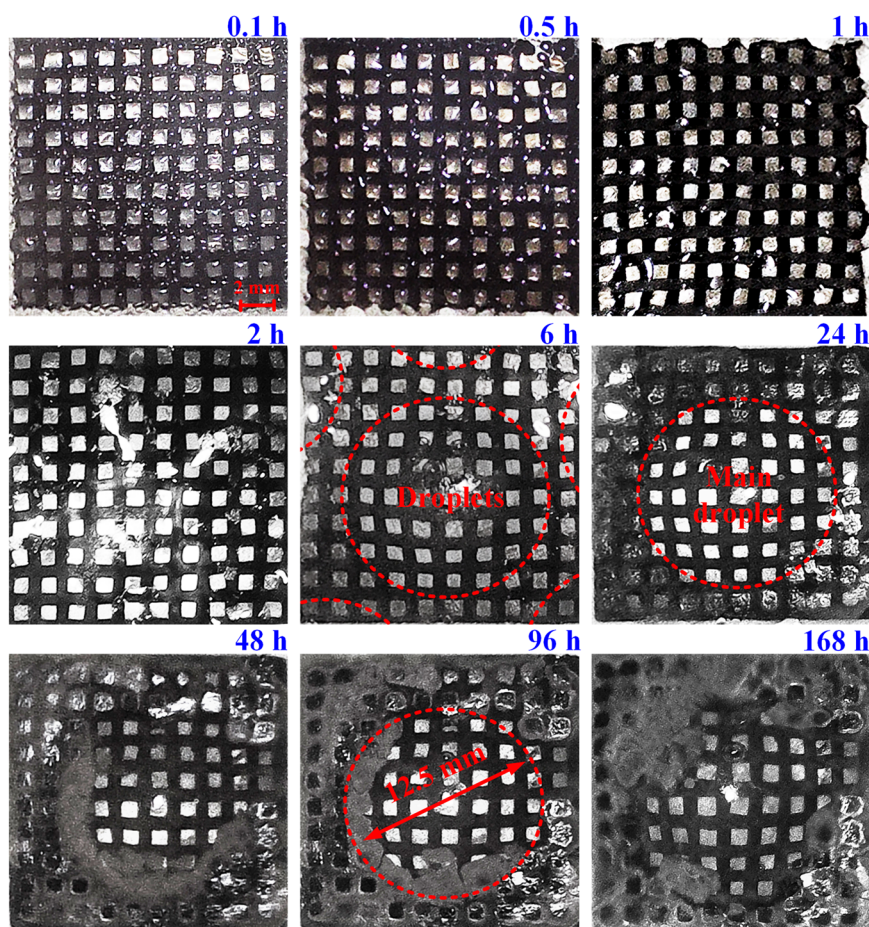


Fig. 1 The formation process of the droplets on the WBE surface. The distribution of the water droplets on the WBE surface photographed by the endoscope at different test periods.

through the intervals of the spikes. It is found that the sudden change of the current on $W_{7,7}$ is more significant than that on $W_{8,10}$, suggesting that the response of the current change on droplet falling is more sensitive for the wire electrodes beneath the droplet. The wire electrode beneath the droplet is more suitable for DRT measurement. Since the distribution and the diameters of the droplets could be revealed from the distribution of the macro-cell current, the WCR is further calculated according to the DRT and the volume of the droplets.

$$\text{WCR} = \frac{\rho_w V}{A_s \text{DRT}} \quad (1)$$

where V is the total volume of the droplets on the WBE surface, ρ_w is the density of condensed water, A_s is the surface area of the WBE, and the measured average DRT is 2300 s. Since the main droplet nearly covered half of the WBE surface, the partial droplets at the corners and edges are neglected in this work to simplify the calculation process. Generally, the shape of the condensed water droplet would present as an approximate hemisphere due to the surface tension². Therefore, the total volume of the droplets could be roughly calculated as:

$$V = \frac{\pi d^3}{12} \quad (2)$$

where d is the diameter of the main droplet. The calculated WCR using WBE is $0.837 \text{ g} \cdot \text{m}^{-2} \cdot \text{s}^{-1}$, which is slightly lower than the real WCR of $0.927 \text{ g} \cdot \text{m}^{-2} \cdot \text{s}^{-1}$ obtained from the condensate collector. The tiny measurement error is induced by the neglect of the partial droplets on the WBE. The comparison results indicate that the WCR could be well evaluated using the WBE technique.

The local electrochemical measurement results on WBE

The location of the droplet and the distribution of the anodes and cathodes on the WBE are visualized from the macro-cell current mapping. Thereafter, the influence of the micro-cell corrosion on TLC was further studied by local LPR measurement. After the compensation of the solution resistance from impedance measurement of high frequency, the micro-cell current (i_{mij}) flowing in a single wire electrode could be calculated as:

$$i_{mij} = \frac{B}{R_{pij}} \quad (3)$$

where B is the Stern-Geary coefficient which is used as 15 mV according to the measured polarization curve in the collected condensed water (the polarization curve is presented in Supplementary Note 3) and R_{pij} is the linear polarization resistance of the selected wire electrode. Since a main droplet formed on the steel surface, the locations of the typical wire electrodes were basically selected according to the distance away from the centre of the droplet. In this way, the influence of the interfacial chemical heterogeneity on micro-cell corrosion could be fully considered. On the other hand, the wire electrodes at the similar distance were further selected according to the macro-cell current distribution to consider the influence of interfacial electrochemical heterogeneity as well.

The distribution of the macro-cell current and the calculated micro-cell current at different test periods are plotted in Fig. 4. More details of the measured LPR and R_s of these typical wires electrodes are presented in Supplementary Note 4. The micro-cell currents of the wire electrodes beneath the droplet were similar

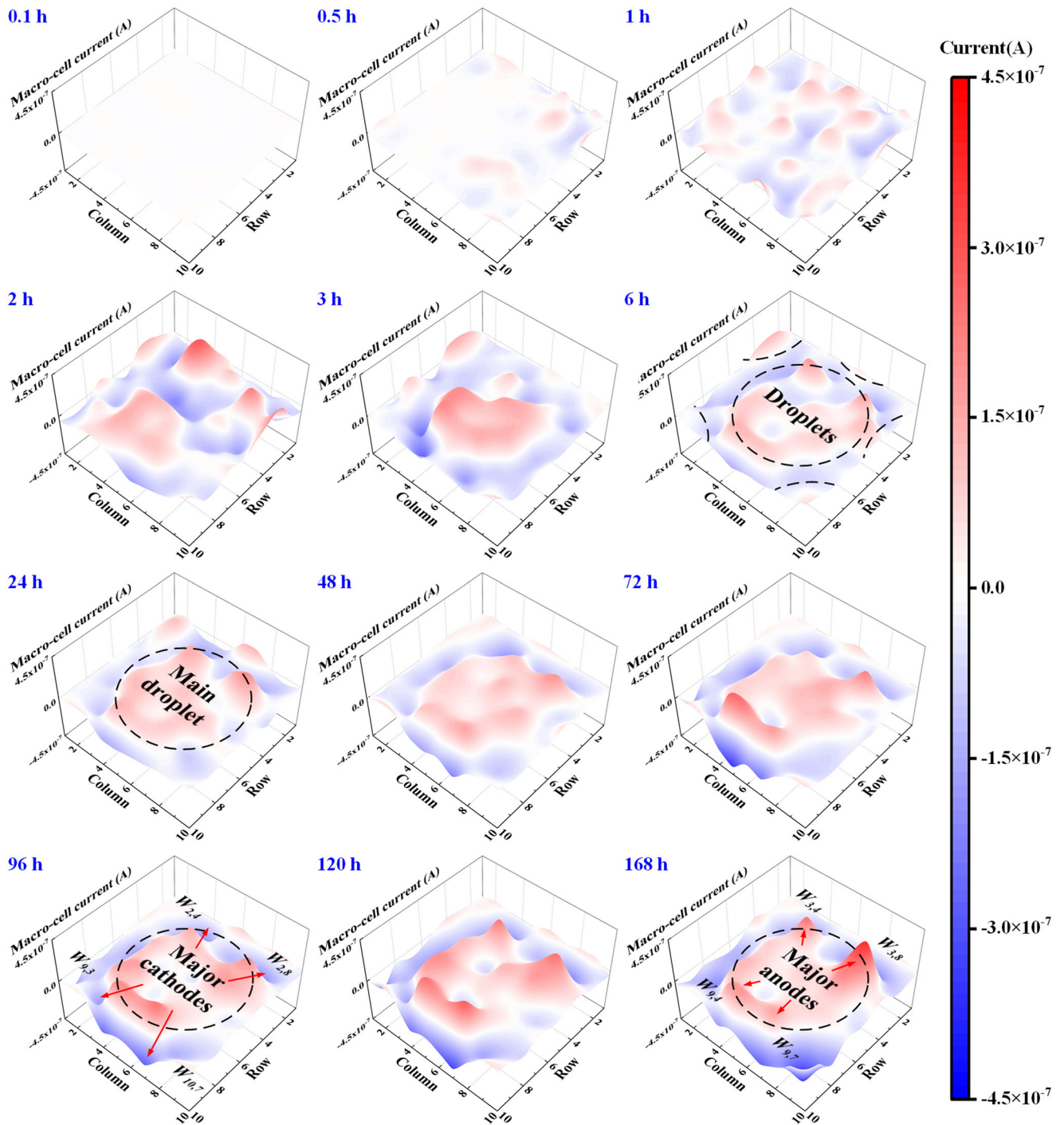


Fig. 2 The macro-cell current distribution maps. The distribution of the macro-cell currents on the WBE at different test durations.

after 24 h of test (Fig. 4a), indicating a relatively uniform micro-cell corrosion beneath the droplet. The micro-cell current of the anodic sites and the cathodic sites beneath the droplets were close, suggesting that the macro-cell current nearly has no influence on the micro-cell corrosion at TLC conditions. The micro-cell currents of the major cathodic sites where were located at the droplet outside were significantly lower than those beneath the droplet. The accurate boundary of the water droplet could be further identified from the local micro-cell currents. The micro-cell currents of the wire electrodes located at the edges of other

droplets ($W_{1,1}$ and $W_{10,10}$) are similar to those beneath the main droplet, indicating that the micro-cell corrosion rate inside of the droplet might be similar.

Along with the corrosion propagation, the wire electrodes beneath the droplets occupied significantly higher micro-cell currents than those outside the droplet (Fig. 3b–d). The micro-cell corrosion rate inside the droplet shows an obvious increase with respect to the distance from the droplet centre at day 3–7. The influences of the macro-cell current on the micro-cell current were still tiny, indicating that the main contributor of the micro-cell

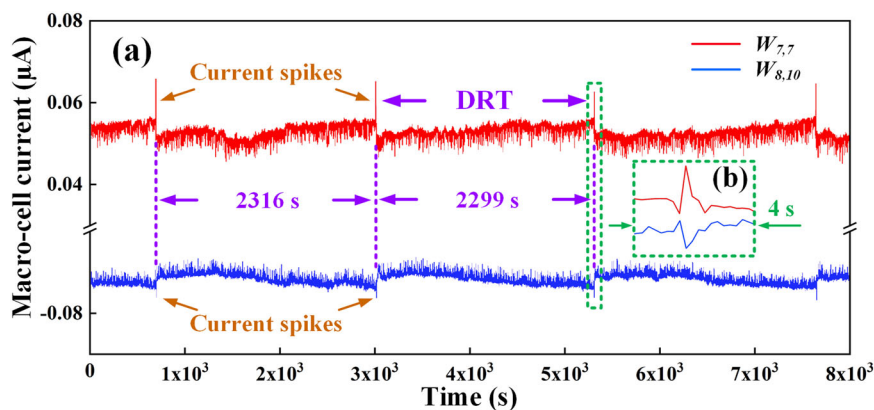


Fig. 3 The dynamic changes of macro-cell currents. **a** Time dependence of the macro-cell currents of $W_{7,7}$ and $W_{8,10}$. **b** The instant current change after droplet falling.

corrosion is the interfacial chemical heterogeneity beneath the droplet. The relationship between the micro-cell current and distance from the centre of the main droplet can be well fitted by quadratic functions. The micro-cell currents of $W_{1,1}$ and $W_{10,10}$ were always close to those of the wire electrodes at the edge of the main droplet. As $W_{1,1}$ and $W_{10,10}$ were also located at the edge of other droplets, it verifies that the micro-cell corrosion performance beneath different droplets would be similar. The micro-cell currents of the wire electrodes outside the droplets were almost the same, suggesting that the micro-cell corrosion performances of the wire electrodes outside the droplets were also similar. According to the local electrochemical measurements, the boundaries of the droplets could be accurately determined. Meanwhile, the micro-cell corrosion rate inside and outside the droplets could be well fitted from the selected typical wire electrodes.

The TLC performance of the steel coupon

Five droplets formed on the steel coupon after 7 days of TLC test (Fig. 5a). The local areas inside and outside the droplets could be clearly identified. The general diameter of the water droplets is 12.2 mm, which is similar to the diameter of the main droplet on WBE. The measured general DRT and WCR of the steel coupon are 2250 s and $0.983 \text{ g} \cdot \text{m}^{-2} \cdot \text{s}^{-1}$, which are also close to the those obtained from WBE test. The average corrosion rate of the steel coupon calculated from weight loss is $0.083 \text{ mm} \cdot \text{y}^{-1}$.

The photo of the steel coupon after the drying of the steel surface is presented in Fig. 5b, which is similar to the surface morphology of the WBE after TLC as shown in Supplementary Fig. 5a. The boundaries of the droplets could be clearly identified from the colour difference. The steel presents a dark colour beneath the droplets and dense corrosion product film is found at the intervals of the droplets. The local morphologies inside of the droplets (Area A and D in Fig. 5b) and outside of the droplets (Area B and C in Fig. 5b) are presented in Fig. 6a–d. The steel surfaces inside the droplet all become rough, indicating the occurrence of serious corrosion. However, a dense corrosion product film is found on the steel surface outside the droplets. The local surface morphologies of the steel coupon are totally the same as those observed on WBE (Supplementary Fig. 5b, e). The comparison results indicate that the WBE sensor could be effectively used to restore the TLC performance on a one-piece electrode.

The corrosion product which is composed by Fe, Fe_3C , and FeCO_3 were detected via the XRD spectra as presented in Supplementary Fig. 6. The EDS results show that the C and O

contents are extremely low at the areas inside of the droplet (Fig. 6e, h), indicating nearly no corrosion products accumulate on the steel surface beneath the droplet (Fig. 6a, d). On the other side, the ion contents shown in Fig. 6f, g suggest that dense FeCO_3 layers cover the local areas outside the droplets (Fig. 6b, c).

DISCUSSION

The calculation of the localized TLC rate using WBE

The WBE measurement results show that the total steel loss of each wire electrode under TLC is induced by both macro-cell current and micro-cell current. The steel loss induced by the macro-cell corrosion could be directly calculated from the anodic current charge of each wire³⁷.

$$d_{Mi,j} = \frac{M \sum i_{Mi,j} \Delta T}{nF\rho_m} \quad (i_{Mi,j} > 0) \quad (4)$$

where $d_{Mi,j}$ is the corrosion depth of $W_{i,j}$ induced by macro-cell corrosion. M is the molecular weight, $i_{Mi,j}$ is the macro-cell current density of $W_{i,j}$ in one measurement circle, ΔT is the time interval of current mapping, n is the number of the transferred electrons, F is the Faraday constant, and ρ_m is the steel density. Figure 7a present the corrosion depth map calculated from the macro-cell current. The local steel loss induced by the macro-cell current is far below the actual steel loss measured by local 3D profiles plotted in Fig. 7b (the measurement procedure of the local corrosion depth is presented in Supplementary Note 7), indicating that the micro-cell corrosion is the main contributor of TLC. This clearly suggests the need for measurement of both local macro-cell corrosion and micro-cell corrosion.

Local linear polarisation was intended for measuring local micro-cell corrosion, however, since all the wire electrodes on the WBE are coupled together during the TLC test, the real potential of each wire would deviate from OCP. Accordingly, the measured micro-cell current ($i_{mi,j}$) using the LPR method could not be directly used to reflect the micro-cell corrosion rate. This issue could be addressed through data analysis based on the Evans diagrams of the wire electrodes under anodic polarization and cathodic polarization (Supplementary Fig. 8). When $W_{i,j}$ is polarized form the corrosion potential ($E_{corri,j}$) to the polarization potential ($E_{pi,j}$), the anodic current density ($i_{ai,j}$) and cathodic current density ($i_{ci,j}$) on $W_{i,j}$ could be expressed as:

$$i_{ai,j} = i_{mi,j} 10^{\frac{E_{pi,j} - E_{corri,j}}{b_a}} \quad (5)$$

$$i_{ci,j} = i_{mi,j} 10^{\frac{E_{pi,j} - E_{corri,j}}{b_c}} \quad (6)$$

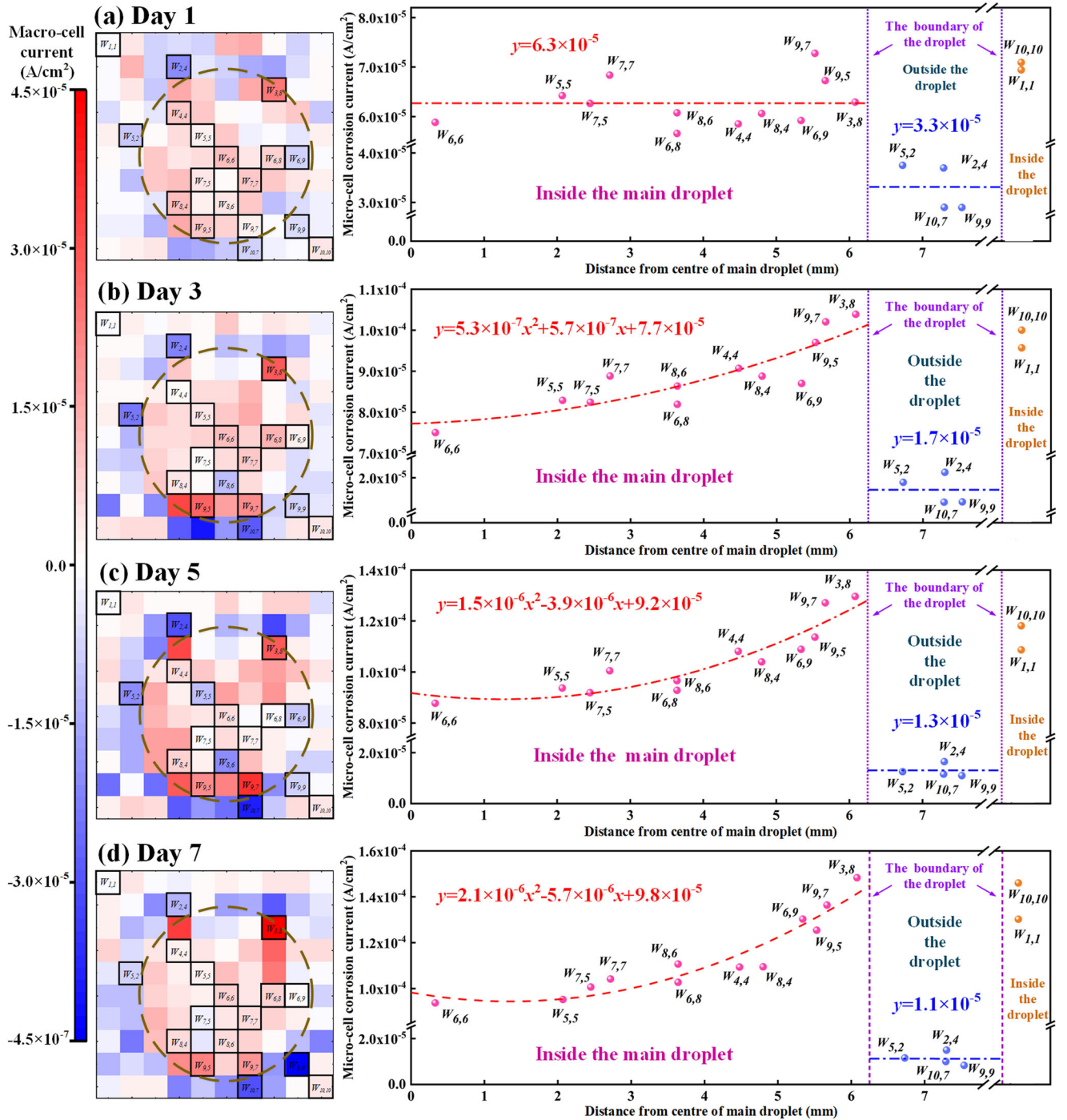


Fig. 4 The selection and local electrochemical measurements of the typical wire electrodes at different locations of WBE. **a** Day 1, **b** Day 3, **c** Day 5 and **d** Day 7.

where the b_a and b_c are the anodic and cathodic Tafel slopes, respectively. In combination of Eq. (5) and Eq. (6), Eq. (7) could be obtained:

$$b_a [\lg(i_{aij}) - \lg(i_{mi,j})] - b_c [\lg(i_{mi,j}) - \lg(i_{ci,j})] = 0 \quad (7)$$

The macro-cell current of W_{ij} could be calculated as:

$$i_{Mij} = i_{aij} - i_{ci,j} \quad (8)$$

Insert Eq. (8) into Eq. (7), Eq. (7) could be written as:

$$b_a \lg\left(\frac{i_{aij}}{i_{mi,j}}\right) + b_c \lg\left(\frac{i_{aij} - i_{mi,j}}{i_{mi,j}}\right) = 0 \quad (9)$$

The real corrosion rate of the W_{ij} could be calculated from i_{aij} . In order to solve i_{aij} , Eq. (9) is rewritten as:

$$i_{aij} = f(i_{aij}) = i_{mi,j} \left(\frac{i_{aij} - i_{mi,j}}{i_{mi,j}}\right)^{-\frac{b_c}{b_a}} \quad (10)$$

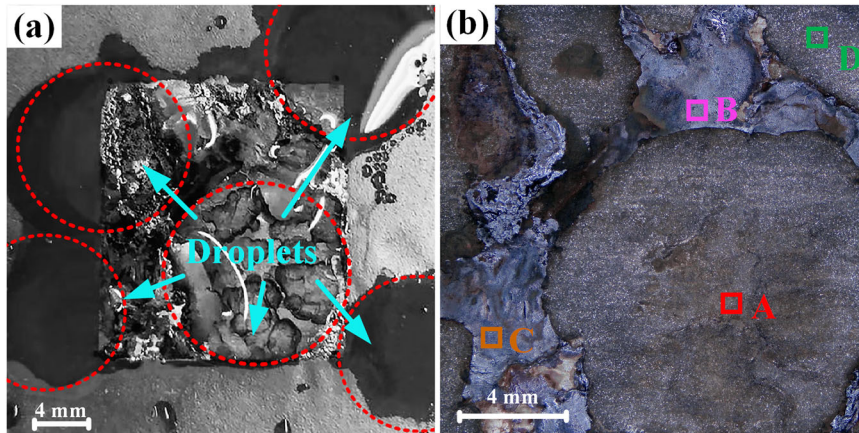


Fig. 5 The photos of the steel coupon. **a** After 7 days of TLC test. **b** After being dried.

The i_{Mij} is directly obtained from the current mapping. The $i_{mi,j}$ could be fitted from the LPR measurement results shown in Fig. 8:

$$\begin{cases} i_{mi,j} = a\rho_{ij}^2 + b\rho_{ij} + c_1 & (W_{ij} \text{ inside of the droplet}) \\ i_{mi,j} = c_2 & (W_{ij} \text{ outside of the droplet}) \end{cases} \quad (11)$$

where ρ_{ij} is the radius between the selected W_{ij} and the centre of the droplet, and a , b , c_1 and c_2 are the fitted constants at different test duration. Since the diameters of the formed droplets are similar (Fig. 5), the diameters of the droplets which covered the corner and edge of the WBE are deemed as the same as the main droplets to simplify the calculation process. The b_a and b_c are fitted from the measured polarization curve in the collected condensed water (see the Supplemental Materials). As a result, the $i_{ai,j}$ could be solved using an iterative method according to Eq. (10):

$$i_{ai,j(k+1)} = f(i_{ai,jk}) \quad (12)$$

where k is the iteration times. The initial value of $i_{ai,j}$ is set as $i_{mi,j}$ and the absolute error bound was set as $1 \times 10^{-10} \text{ mA}\cdot\text{cm}^{-2}$.

After the calculation of $i_{ai,j}$, the modified corrosion depth of each wire electrode could be calculated from Eq. (4) by replacing i_{Mij} with $i_{ai,j}$. The calculation results of the total corrosion depth ($d_{ti,j}$) induced by both macro-cell corrosion and micro-cell corrosion are shown in Fig. 8a. The measurement error ($\Delta_{i,j}$) of the corrosion depth calculated from $i_{ai,j}$ is depicted in Fig. 8b.

$$\Delta_{i,j} = d_{ti,j} - d_{ri,j} \quad (13)$$

where $d_{ri,j}$ is the real corrosion depth of each wire electrode directly measured from local 3D profiles. The localized corrosion is overestimated inside of the droplet and underestimated outside the droplet (Fig. 8b). The measurement error is possibly induced by the inhomogeneous chemical environment on the WBE surface. The polarization curve measured from the immersion test could not totally reveal the electrochemical behaviour beneath the water droplet. On the other hand, the uneven distribution of the FeCO_3 film on the WBE would also lead to the change of local electrochemical kinetic parameters, resulting in the occurrence of measurement error. However, the largest measurement error is $<5 \mu\text{m}$ as shown in Fig. 8b. The calculated highest corrosion depths of the wire electrodes are $30.0 \mu\text{m}$, $29.0 \mu\text{m}$, $27.3 \mu\text{m}$ and $26.8 \mu\text{m}$ ($W_{9,4}$, $W_{3,8}$, $W_{9,7}$ and $W_{8,3}$), respectively, which is almost the same as the real corrosion depths of $28.6 \mu\text{m}$, $28.5 \mu\text{m}$, $25.7 \mu\text{m}$ and $24.9 \mu\text{m}$. The compared results indicate that the localized corrosion of TLC could be well probed by the modified WBE.

These results suggest that the WBE technique has limitations in accurately measuring the localized corrosion rate when the micro-

cell corrosion becomes the important contributor to the localized steel degradation. The micro-cell corrosion always occurs in the scale of micron or nanometre which could not be directly probed by WBE due to the dimensional limitation of the wire electrodes. Normally, the micro-cell current could be compensated from the coupled potential measurement or using WBE-EN technique³⁸. However, the local polarized potential and the OCP of the wire electrodes are hard to be probed at TLC conditions. Consequently, the conjunction of the macro-cell current mapping and micro-cell current measurement provides a method to overcome the difficulties in probing the localized corrosion when the potential mapping is hard to be realized on the WBE.

The initiation and propagation of TLC

The test results show that the corrosion performance of the steel inside of the droplet is significantly different from that outside the droplet. This is believed to be closely related to differences in the precipitation of the corrosion product inside and outside the droplets. Therefore, exploring the formation and deposition process of the FeCO_3 layer on the steel surface could facilitate understanding the initiation and propagation of TLC under sweet corrosion^{4,39,40}. It is known that the FeCO_3 crystals could only begin to precipitate when the ions concentration product of Fe^{2+} and CO_3^{2-} exceed the solubility product (K_{sp})⁴¹:

$$S_S = \frac{c_{\text{Fe}^{2+}} c_{\text{CO}_3^{2-}}}{K_{sp}} \quad (14)$$

where S_S is the supersaturation of ferrous carbonate, the $S_S > 1$ is the basic requirement for the precipitation of FeCO_3 crystal⁴². The K_{sp} could be calculated according to the reference⁴¹:

$$K_{sp} = 10^{-59.3498 - 0.0413777T_k - \frac{2.1963}{T_k} + 24.5724 \log(T_k) + 2.518I^{0.5} - 0.657I} \quad (15)$$

where T_k is the temperature (K) of the condensed liquid which is employed as 317 K, I is the ionic strength which is normally deemed as 0 for TLC cases due to the extremely low ion concentrations⁴³. The calculated K_{sp} is $9.44 \times 10^{-12} \text{ kmol}^2 \cdot \text{m}^{-6}$ at the employed test condition.

A thick and dense FeCO_3 layer is found outside the droplet, leading to the mitigation of the micro-cell corrosion and cathodic protection of the local areas. Apparently, the occurrence of the corrosion outside the droplet could lead to the quick accumulation of the Fe^{2+} and CO_3^{2-} in the thin liquid film, resulting in a high S_S and the precipitation of dense FeCO_3 crystals outside the droplet. Although significant higher corrosion rates are registered on the wire electrodes inside of the droplet, the continuous renewal of the droplets would take away the generated Fe^{2+} and CO_3^{2-} , leading to the fluctuation of the S_S inside of the droplets.

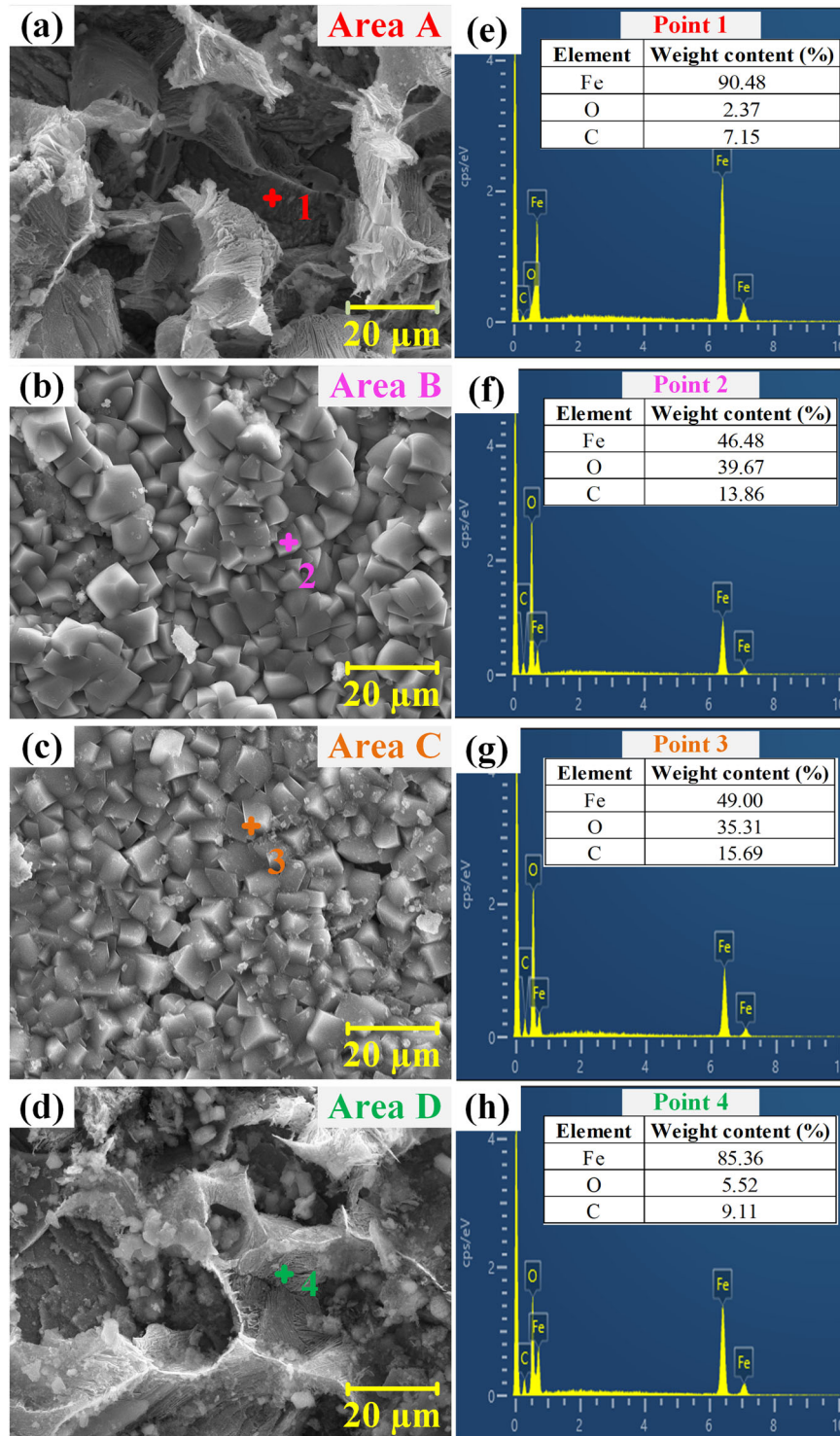


Fig. 6 SEM images and EDS results of typical areas. SEM images of the local areas marked in Fig. 5b **a** Area A, **b** Area B, **c** Area C, **d** Area D and the EDS results of local points in the SEM images **e** Point 1, **f** Point 2, **g** Point 3, **h** Point 4.

Therefore, the highest S_5 is calculated to estimate the formation process of the FeCO_3 layer beneath the droplets. Assuming that the fall of the droplet could take away most of the Fe^{2+} , the general concentration of the Fe^{2+} would reach the peak value before the droplet falling. The general concentration of Fe^{2+} ($c_{\text{Fe}^{2+}}$) in the main droplet could be quantitatively calculated according to the anodic dissolution rate, DRT and the volume of

the droplet:

$$c_{\text{Fe}^{2+}} = \frac{\sum_{i,j} i_{a,i} A_{i,j}}{nFV} DRT \quad (16)$$

where $\sum_{i,j} i_{a,i} A_{i,j}$ is the sum of the anodic current beneath the main droplet which could be obtained from the WBE measurement results, $A_{i,j}$ is the surface area of $W_{i,j}$ beneath the main droplet. The $A_{i,j}$ is equal to the surface area of a whole wire electrode when $W_{i,j}$

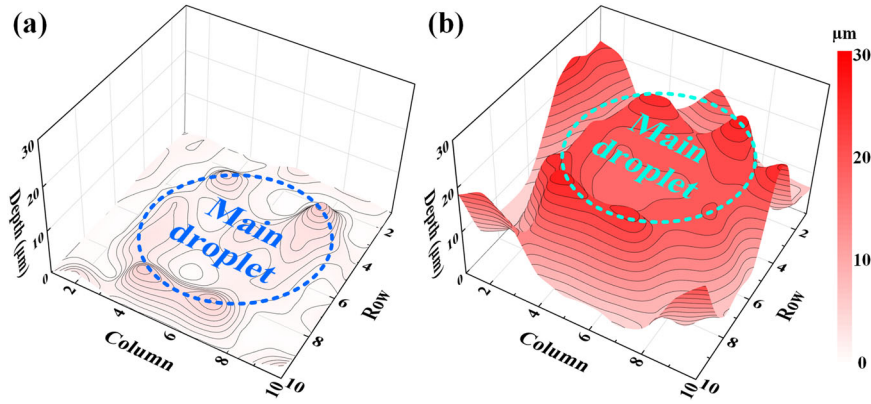


Fig. 7 The calculated corrosion depth. The map of the corrosion depth calculated from **a** macro-cell current and **b** local 3D profiles.

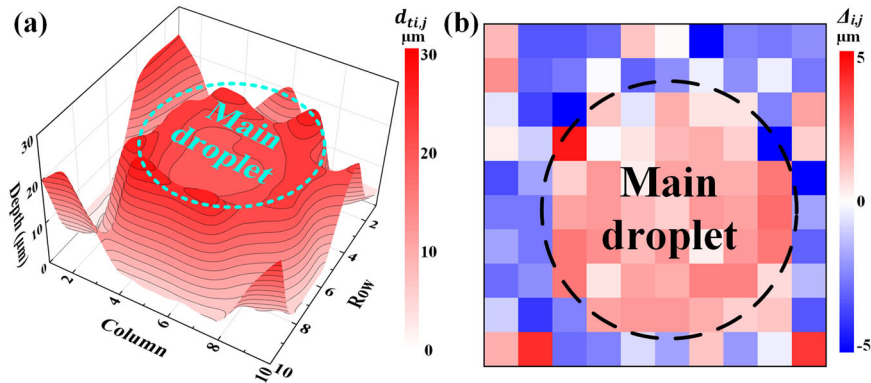


Fig. 8 The calculated corrosion depth and the measurement error. **a** The corrosion depth map calculated from the i_{aij} . **b** The measurement error between the calculated value and the real corrosion depth measured by 3D profiles.

Table 1. The definition and the calculation results of the equilibrium constants.

Equilibrium constant	Value
$K_{sol} = \frac{14.5}{1.00258} 10^{-(2.27+5.65 \times 10^{-3}T_f - 8.06 \times 10^{-6}T_f^2 + 0.075I)}$	2.26×10^{-2}
$K_{hyd} = 2.58 \times 10^{-3}$	2.58×10^{-3}
$K_{ca} = 387.6 \times 10^{-(6.41-1.594 \times 10^{-3}T_f + 8.52 \times 10^{-6}T_f^2 - 3.07 \times 10^{-5}p - 0.4772p^{0.5} + 0.11807I)}$	2.06×10^{-4}
$K_{bi} = 10^{-(10.61-4.97 \times 10^{-3}T_f + 1.331 \times T_f^2 - 2.624 \times 10^{-5}p - 1.66p^{0.5} + 0.34661I)}$	6.04×10^{-11}
$K_{wa} = 10^{-(29.3868-0.0737549T_k + 7.47881 \times 10^{-5}T_k^2)}$	3.22×10^{-14}

is totally beneath by the droplet. Meanwhile, the concentration of the CO_3^{2-} ($c_{\text{CO}_3^{2-}}$) could be calculated based on the following chemical reactions^{44,45}:

$$c_{\text{CO}_3^{2-}} = \frac{K_{sol}K_{hyd}K_{ca}K_{bi}p_{\text{CO}_2}}{c_{\text{H}^+}^2} \quad (17)$$

$$\text{CO}_2(\text{g}) \leftrightarrow \text{CO}_2(\text{aq}) \quad K_{sol} = \frac{c_{\text{CO}_2}}{p_{\text{CO}_2}} \quad (18)$$

$$\text{CO}_2 + \text{H}_2\text{O} \leftrightarrow \text{H}_2\text{CO}_3 \quad K_{hyd} = \frac{c_{\text{H}_2\text{CO}_3}}{c_{\text{CO}_2}} \quad (19)$$

$$\text{H}_2\text{CO}_3 \leftrightarrow \text{H}^+ + \text{HCO}_3^- \quad K_{ca} = \frac{c_{\text{HCO}_3^-}c_{\text{H}^+}}{c_{\text{H}_2\text{CO}_3}} \quad (20)$$

$$\text{HCO}_3^- \leftrightarrow \text{H}^+ + \text{CO}_3^{2-} \quad K_{bi} = \frac{c_{\text{CO}_3^{2-}}c_{\text{H}^+}}{c_{\text{HCO}_3^-}} \quad (21)$$

$$\text{H}_2\text{O} \leftrightarrow \text{H}^+ + \text{OH}^- \quad K_{wa} = c_{\text{H}^+}c_{\text{OH}^-} \quad (22)$$

where K_{sol} , K_{hyd} , K_{ca} and K_{bi} are the reaction equilibrium constants whose definitions and calculation results are listed in Table 1, p_{CO_2} is the partial pressure of the CO_2 which is about 0.85 bar, c_{H^+} is the

concentration of the hydrogen ions. To ensure the electro-neutrality of the solution, the charge of the cations should equal to the charge of anions:

$$2c_{\text{Fe}^{2+}} + c_{\text{H}^+} = c_{\text{HCO}_3^-} + 2c_{\text{CO}_3^{2-}} + c_{\text{OH}^-} \quad (23)$$

In combination of Eq. (17) and Eq. (23), Eq. (24) is obtained:

$$c_{\text{H}^+}^3 + 2c_{\text{Fe}^{2+}}c_{\text{H}^+}^2 - (K_{wa} + K_{sol}K_{hyd}K_{ca}p_{\text{CO}_2})c_{\text{H}^+} - 2K_{sol}K_{hyd}K_{ca}K_{bi}p_{\text{CO}_2} = 0 \quad (24)$$

The c_{H^+} could be solved from Eq. (24). Thereafter, the $c_{\text{CO}_3^{2-}}$ and S_5 inside of the droplet could be calculated using Equation (17) and Eq. (14). The variations of the pH and the S_5 inside of the droplet during the 7 days of test is plotted in Fig. 9.

The pH of the droplet kept increasing from 5.1 to 5.3 during the 7 days of TLC test (Fig. 9a), indicating that the cathodic reaction involves the reduction of H^+ , H_2CO_3 and HCO_3^- ⁴⁶. Along with the solution pH increasing, the S_5 inside of the droplet presents a dramatic increase from 0.57 to 3.41 after 7 days of test (Fig. 9b).

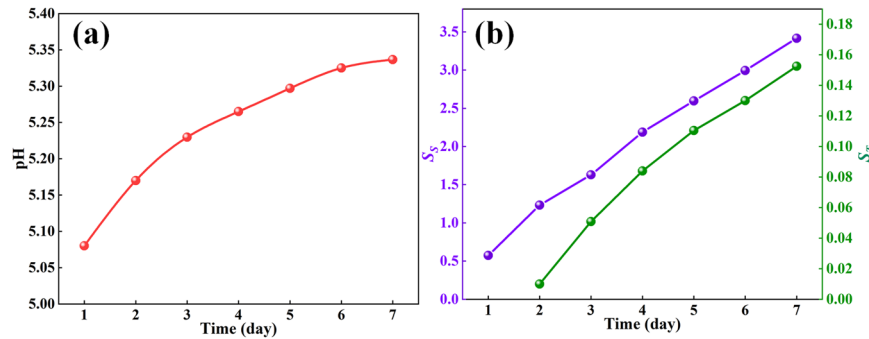


Fig. 9 The calculation results of pH and supersaturation. **a** Time dependence of the solution pH. **b** Time dependence of the supersaturation inside of the droplet.

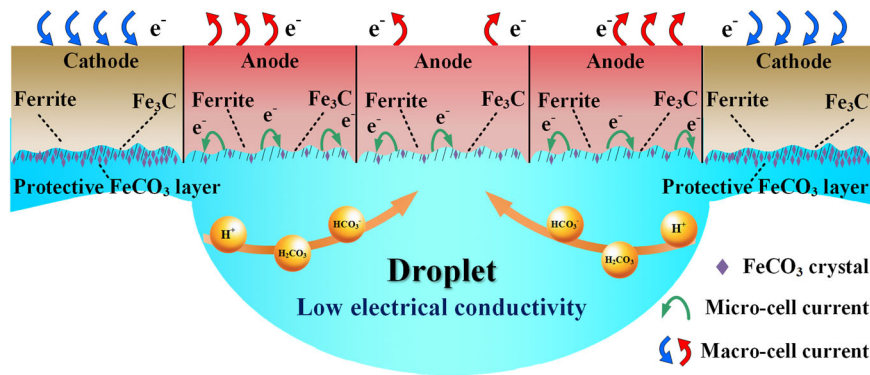


Fig. 10 Schematic diagram of TLC at the test condition. The mechanistic model of the distribution of the corrosion products and the formation of macro-cell currents.

The S_T becomes >1 after 2 days of test, indicating that the presentation of the FeCO_3 layer could also occur beneath the droplet in the following test period. The form of the FeCO_3 layer beneath the droplet is further estimated using the scaling tendency (S_T) which is a non-dimensional parameter^{41,46}:

$$S_T = \frac{R_{\text{CLA}}}{\text{CR}} \quad (25)$$

where CR is the general corrosion rate beneath the main droplet, R_{CLA} is the accumulation rate of corrosion layer:

$$\text{CR} = \frac{\sum i_{\text{aij}} A_{i,j}}{nF \sum A_{i,j}} \quad (26)$$

$$R_{\text{CLA}} = K_r K_{\text{sp}} (S_T - 1) \quad (27)$$

where K_r is a kinetic constant which could be calculated using an Arrhenius' type equation:

$$K_r = e^{A - \frac{B_a}{RT}} \quad (28)$$

where A is the pre-exponential factor which is typically used as 28.4 according to the reference⁴¹, B_a is the apparent activation energy equals to $64851 \text{ J} \cdot \text{mol}^{-1}$, and R is the gas constant equals to $8.314 \text{ J} \cdot \text{mol}^{-1} \cdot \text{K}^{-1}$. In combination of Eqs. (25)–(28), the dynamic change of the S_T is calculated and plotted in Fig. 9b. The S_T shows an obvious increase from 0.01 to 0.15 after 7 days of immersion. However, the highest S_T is still much <1 , suggesting that porous and non-protective corrosion product is likely to form beneath the droplets⁴². Since the adhesion strength of the porous FeCO_3 layer is rather poor⁴³, the corrosion product would peel from the steel surface due to the gravity and the disturbances of droplet falling. In addition, the continuous renewal of the water droplet could also retard the nucleation of the FeCO_3 crystal, further delaying the film formation beneath the droplet⁴. As a result, only few FeCO_3 crystals and a small

amount of amorphous corrosion products are observed inside of the droplets.

On the basis of the WBE measurement results and the environmental parameters, the formation process and the scaling tendency of the FeCO_3 layer could be well analysed. Thereafter, the dynamic progression of TLC is further discussed according to the discrepancy of film formation inside and outside the droplet. The distribution of both micro-cell currents and macro-cell currents inside and outside the droplet is schematically depicted in Fig. 10. As no dense and protective FeCO_3 formed on the steel surface inside of the droplet, the corrosion rate kept relatively high beneath the droplets. It is known that the eutectoid ferrite would act as the anodes due to the lower potential than Fe_3C in the pearlite⁴⁷. The preferential dissolution of ferrites in X65 pipeline steel would result in the accumulation of the Fe_3C layer on the steel surface (Fig. 11a). The remained Fe_3C layer could enhance the micro-cell corrosion, leading to the continuous increase of the micro-cell current beneath the droplets (Fig. 11a). As the corrosion propagation is significantly influenced by the mass transfer process in TLC cases, the micro-cell corrosion beneath the droplets is determined by the diffusion of H^+ , H_2CO_3 and HCO_3^- in the condensed water film. The steel located close to the inside boundary of the droplet would suffer higher micro-cell corrosion rates due to the thinning of the water film and the enhanced cathodic reaction. Accordingly, the increase of the micro-cell current is found along with the distance increasing of the wire electrode to the droplet centre. The micro-cell corrosion of the wire electrodes outside the droplets dropped quickly due to the formation of the dense and protective FeCO_3 (Fig. 11b). No obvious difference in the micro-cell current on the wire electrodes is found, indicating that the mass transfer process in the thin liquid film is relatively uniform.

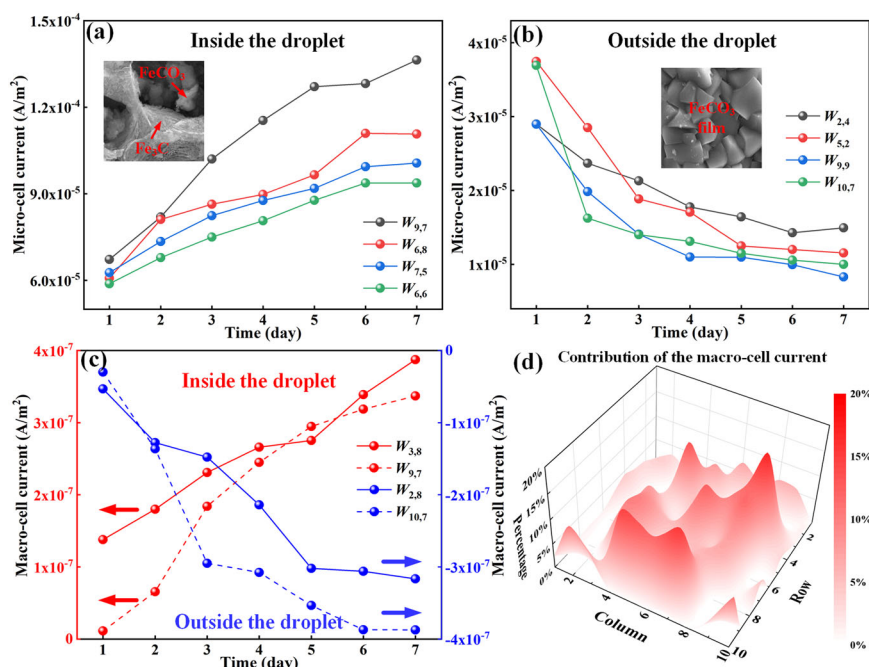


Fig. 11 The evolution of micro-cell currents and macro-cell currents. **a** Time dependence of the micro-cell current of typical wire electrodes beneath the droplet. **b** Time dependence of the micro-cell current of typical wire electrodes outside the droplet, **c** Time dependence of the macro-cell current of typical electrodes around the boundary of the droplet. **d** The contribution of the macro-cell current of the total corrosion loss of each wire electrode.

The formation of the protective FeCO_3 on the steel outside the droplets also enhanced the macro-cell corrosion on the steel surface. The local areas outside the droplets would act as the major cathodic sites due to the protective film^{48–50}. While, the steel inside of the droplets would become the major anodic sites. Due to the low concentration of the ions in the condensed water, the electrical conductivity of the water droplet is low. The high solution resistance resulted in that the main anodic sites all concentrated at the inside boundary of the droplet where was close to the major cathodes. Both the anodic currents and cathodic currents of the major cathodes and anodes show significant increases in the 7 days of test (Fig. 11c). It indicates that the growing of the protective FeCO_3 layer outside the droplets results in the enhancement of macro-cell corrosion. In order to further understand the contribution of macro-cell current on the TLC, the proportion of the total steel loss induced by macro-cell corrosion ($p_{i,j}$) is calculated and plotted in Fig. 11d.

$$p_{i,j} = \frac{d_{M,i}}{d_{n,j}} \quad (29)$$

The highest contribution of the macro-cell corrosion to the total steel loss is about 20% which occurs on the wire electrodes at the inside boundary of the main droplet (Fig. 11d). Although most of the steel loss under TLC is induced by the micro-cell corrosion, the contribution of the macro-cell corrosion could not be neglected in this case. According to the discussion, it is found that the contribution of both macro-cell corrosion and micro-cell corrosion on TLC could be simultaneously and quantitatively analysed by using the modified WBE sensor.

It should be noted that the experiment and analysis described above are only for the demonstration and illustration of this TLC measurement method under a specific set of TCL testing conditions, more work is needed to assess TLC behaviour under different experimental conditions with and without the presence of corrosion inhibitors. For instance, it is expected that different sizes and shapes of water droplets would form under different conditions, significantly affecting corrosion processes, patterns

and kinetics. The presence of corrosion inhibitors would also lead to significant changes in the corrosion behaviour under water droplets. These will be reported in the future.

In summary, a method has been developed for probing the TLC of pipeline steel based on the use of a modified WBE in conjunction with local electrochemical measurements. The method of combining macro-cell current mapping and micro-cell current measurement overcomes the difficulties in probing the localized corrosion in thin water layers and water drops. On the basis of the measurement results using the modified WBE technique, the following conclusions are drawn: (1) Through the specially designed modified WBE, both the macro-cell current and micro-cell current of each wire electrode could be measured for determining TLC behaviour and kinetics. The location of the droplets is clearly reflected from the distribution of the major anodic sites and the cathodic sites. The macro-cell corrosion can be determined by the WBE current mapping, while micro-cell corrosion is measured by local LPR measurements. In addition, the DRT and the WCR are calculated due to the continuous measurement of the local macro-cell current inside of the droplet. (2) The localized corrosion depths calculated from the method proposed in this work is in agreement with the real corrosion depths measured by local 3D profiles. Based on this method, the contributions of micro-cell corrosion and macro-cell corrosion on total steel loss could be separated. The calculation results show that the micro-cell corrosion is the main contributor to TLC under the experimental condition. (3) The precipitation and the scaling tendency of the FeCO_3 layer inside of the droplet are estimated on the WBE measurement results in conjunction with environmental parameters. Although the calculated S_5 is >1 inside of the droplet after 2 days of test, only porous and non-protective corrosion product film could deposit inside of the droplet due to the extremely lower S_7 . The gravity and the disturbance induced by droplet falling could result in the peeling of the corrosion product, leading to the remaining of few FeCO_3 crystals and amorphous corrosion products inside of the droplets. While, dense and protective FeCO_3 film could form outside the droplets, leading to

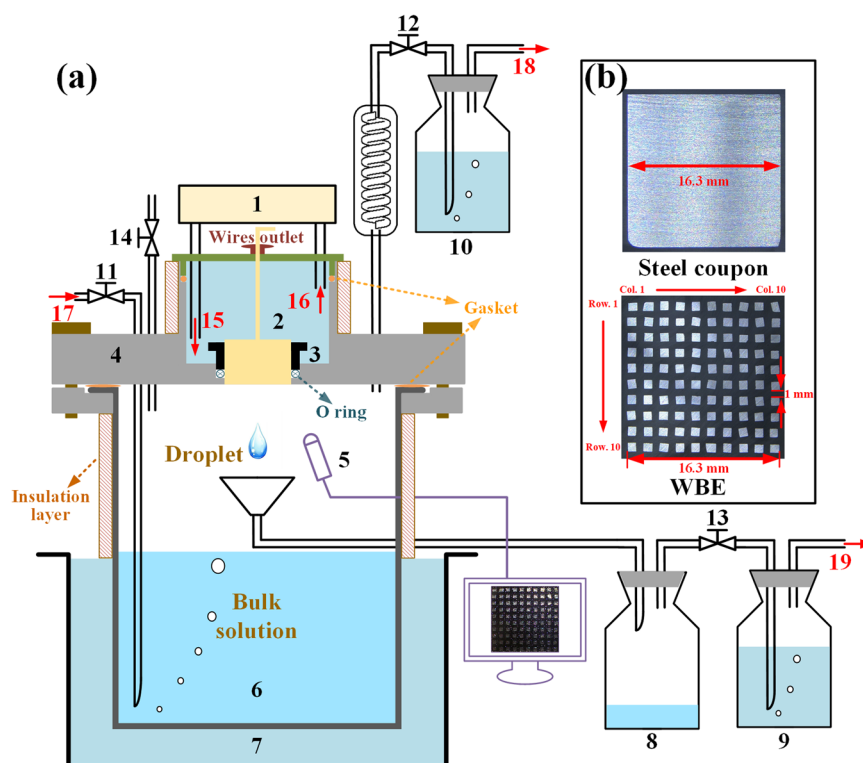


Fig. 12 The test setup used for TLC experiments and the test materials. **a** The schematic diagram of the TLC simulation system. **b** The steel coupon and the WBE used in the test. (1 Cooling system, 2 cooling chamber, 3 sample holder, 4 PTFE lid, 5 endoscope, 6 test cell, 7 water bath, 8 condensate collector, 9–10 Dreschel bottle, 11–14 valves, 15 cooling water inlet 16 cooling water outlet, 17 CO₂ inlet, 18–19 CO₂ outlet.).

the areas beneath the droplets becoming the anodes. (4) The major anodic sites would concentrate at the inside boundary of the droplet due to the high solution resistance of the condensed water. The highest proportion of the macro-cell corrosion could reach 20% of total steel loss on these major anodic sites, indicating that the macro-cell corrosion could not be neglected for TLC. The micro-cell corrosion rate is relatively low and stable outside the droplet due to the formation of dense protective film. While, the micro-cell corrosion rate shows an obvious increase with respect to the distance from the droplet centre, which is caused by the enhanced diffusion of H⁺, H₂CO₃ and HCO₃⁻ along with the tinning of the liquid film from the droplet centre to edge.

METHODS

Materials and test setup

The schematic diagram of the TLC test setup is plotted in Fig. 12a. The test setup is mainly composed of a water bath (Lichen-HH, China), a cylinder glass cell and a cell lid with cooling system. The diameter and the height of the glass cell are 160 mm and 200 mm, respectively, which could store 2 L test solution. During the TLC test, the glass cell is placed in the water bath which could control the solution temperature from room temperature to 100 °C, simulating the hot vapour environment. Carbon dioxide is continually injected into the glass cell through the gas inlet and outlet. To prevent the backflow of air, the CO₂ outlets are sealed by Dreschel bottles containing saturated bicarbonate solution. The cell lid which also works as the sample holder is made of polytetrafluoroethylene (PTFE). The crevice between the cell lid and the glass cell is sealed by a gasket to avoid the leakage. The test sample and the WBE sensor are installed on the sample holder through the reserved hole at the centre of the lid. The interval between the sample and the lid is sealed by an O ring. A cooling chamber is arranged on the back side of the cell lid. The cooling

chamber is constructed by part of the cell lid and a chamber cover. The crevice between the chamber wall and the chamber cover is also sealed by a gasket. The wires of the sample could pass out the cooling chamber through the wire outlet on the chamber cover. The cooling water is injected and circulated into the cooling chamber using a chiller plant (Julabo F25-ME, Germany). The backside temperature of the sample could be adjusted from 0–60 °C in order to simulate the lower temperature side of the pipe wall. The glass cell and the whole cooling chamber are wrapped by thermal insulation layers to maintain stable temperatures of both vapour and cooling water. Besides the main compositions of the test setup, a condensate collector and an endoscope are fixed in the test cell to obtain more information of TLC. The condensate collector is placed 80 mm right beneath the test sample to collect the dripped water droplet. The endoscope (Jiean IV-C40, China) is used to observe the distribution of the condensation water on the sample surface during the experiment.

In this work, both WBE and steel coupons were used to study the initiation and propagation of TLC. The photos of the WBE and the test coupon are presented in Fig. 12b. The WBE and the steel coupon are made of X65 pipeline steel which chemical compositions were 0.04 C, 0.2 Si, 1.5 Mn, 0.011 P, 0.003 S, 0.02 Mo, and Fe balance. The WBE is fabricated by 100 wire electrodes which surfaces are machined in the sizes of 1 × 1 mm. The wire electrodes are numbered as W_{ij} according to their location, where i is the row number and j is the column number. Copper wires are soldered on the back side of the tiny electrodes for electrical connection. The interval between the neighbouring electrodes is 0.7 mm, leading to the total WBE width of 16.3 mm. The side length of the steel coupon is also machined as 16.3 mm which is the same as that of WBE. The same size of the steel coupon with the WBE could provide a basic reference of the condensation process and the TLC performance, aiming to verify whether WBE could be effectively used to mimic a one-piece electrode for TLC

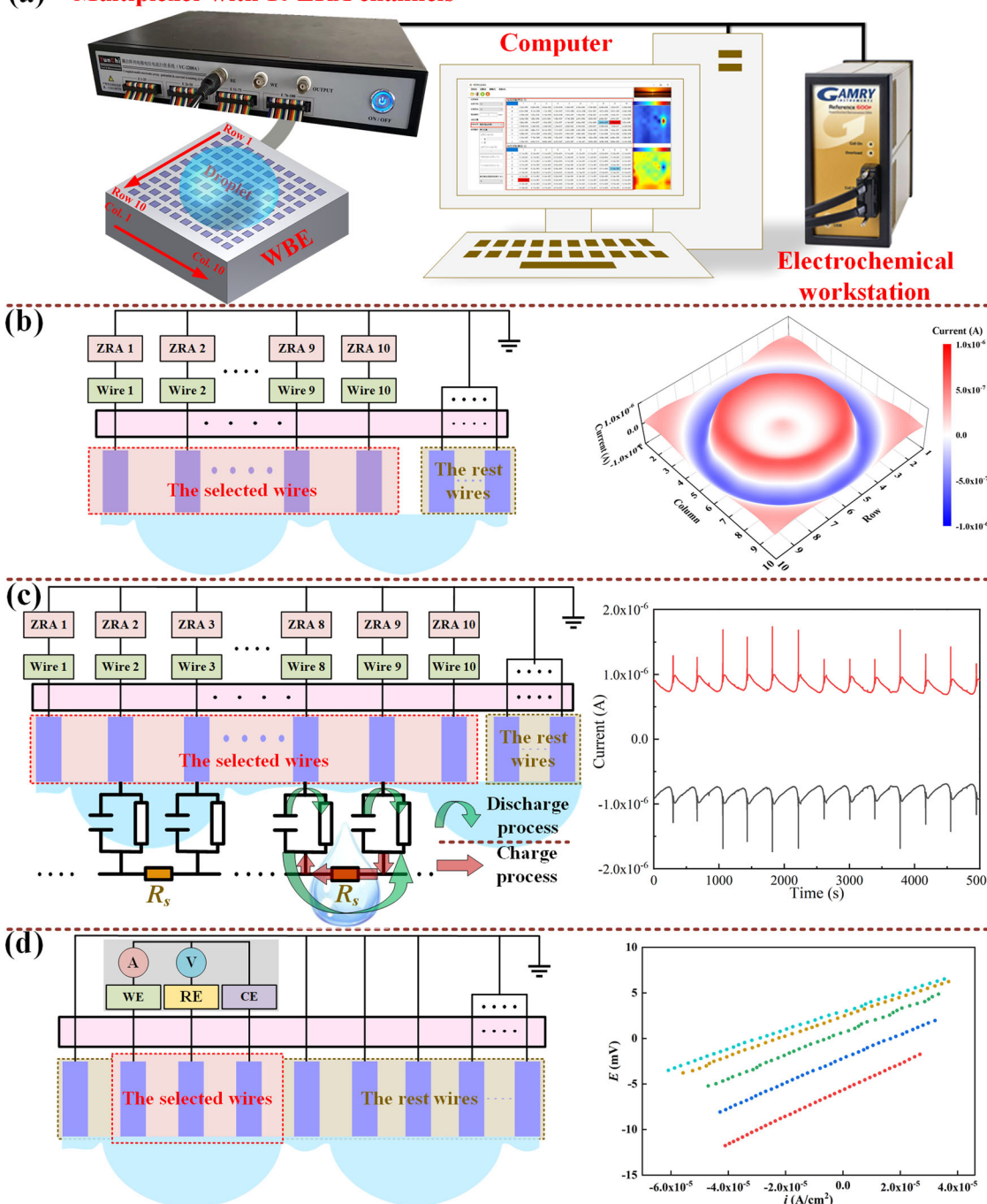
(a) Multiplexer with 10 ZRA channels

Fig. 13 The WBE sensor system used for TLC experiments. **a** Schematic diagram of the WBE sensor system. **b** The measurement circuit of the macro-cell current distribution. **c** The measurement circuit of DRT. **d** The local electrochemical measurement of the selected wire electrodes.

studies. The WBE and the steel coupon were sealed in a cylindrical acrylic tube with the diameter of 50 mm using epoxy resin. The exposed surfaces of the WBE and steel coupon were successively polished by silicon carbide papers from 400 grit to 1200 grit. The polished surfaces were degreased by acetone and rinsed by deionized water before the test.

The measurement principle of the modified WBE system

In order to probe the initiation and propagation of TLC, a modified WBE sensor system as shown in Fig. 13a is fabricated on the basis of traditional WBE technique. In the modified WBE sensor system,

the distribution of the macro-cell current (the current flowing among the wire electrodes) on WBE could be measured by an YC-2200A multiplexer (YunChi, China) containing 10 zero resistance ammeters (ZRA). Besides the macro-cell current mapping of the whole WBE, the macro-cell currents of any selected wire electrodes (up to 10 wires) could be continually measured. In addition, any three or four wire electrodes could be selected from the WBE matrix for local electrochemical measurement. The electrochemical measurements were performed using a Reference 600+ electrochemical workstation (Gamry, US). These functions of the modified WBE system could facilitate visualizing the formation

Table 2. Test parameters of TLC.

Items	Applied parameters
Test Pressure	1.013×10^5 Pa
Test solution	Deionized water with saturated CO ₂
Cooling temperature	45 ± 0.1 °C
Solution temperature	65 ± 0.1 °C
Gas temperature	56 ± 0.1 °C
Test duration	7 days

of the condensed water droplet, probing the DRT and investigating the local electrochemical reaction.

It is known that the formation of the water droplet on the steel surface could lead to the separation of the anodic sites and cathodic sites due to the inhomogeneous mass transfer process beneath the water droplet³⁵. The location and the diameter of the water droplet could be roughly investigated from the macro-cell current distribution. Unlike the water droplet generated on a faced-up steel plate, the droplet formed on the top of the pipe would fall off when the gravity is greater than surface tension. Once the DRT is short, the frequent detachment of the droplet would significantly influence the macro-cell current mapping. Accordingly, the multiplexer with 10 channel ZRAs is employed in the modified WBE system, aiming to probe the macro-cell current distribution in a short period. The application of 10 channel ZRAs could reveal the quick change of the interfacial electrochemical heterogeneity. During the macro-cell current mapping of TLC, the terminals of the 100 wire electrodes are all connected together to mimic a one-piece electrode (Fig. 13b). The current distribution could be measured by switching the 10 ZRAs in connection of all the wire electrodes in 3 s, which greatly shortened the mapping duration. Thereafter, the formation process and the location of the water droplet on the WBE could be well identified. Along with the locating of the water droplet from the macro-cell current distribution map, the wire electrodes located at both anodic sites and cathodic sites could be selected for continuous macro-cell current monitoring (Fig. 13c). The fall and renewal of the water droplet would lead to an obvious modification of the interfacial status, resulting in discharging and charging of the double electrical layer capacitor⁵¹. Accordingly, the DRT could be obtained from the interval of the measured current spikes. Thereafter, the condensation rate could be further evaluated on the basis of the measured DRT.

The macro-cell corrosion performance on the WBE could be well probed from the distribution of anodic and cathodic currents. However, the corrosion caused by the micro-cell current (the internal corrosion current flowing in a single electrode) cannot be revealed by the monitored macro-cell current. Meanwhile, the interfacial reaction and the corrosion resistance at the local area could not be accurately reflected only from the macro-current mapping. As a result, the tiny wire electrodes on the WBE could be selected for local electrochemical measurements via the multiplexer (Fig. 13d). Since the location and the coverage of the droplet are identified from the distribution of the macro-cell current, it could ensure that the selected electrodes are all located in the droplet to avoid the measurement error. Accordingly, the difficulties in selecting the suitable electrodes for local electrochemical measurements could be overcome.

Test procedure

Experiments using both WBE and steel coupon were conducted in a CO₂ saturated environment. The test conditions are listed in Table 2. In the preparation period, the deionized water was deoxygenated by continuous CO₂ sparging of 24 h. The test

solution was pre-heated to 65 °C before the test. The CO₂ was also pre-introduced into the test cell for 4 h to avoid the oxygen contamination. Meanwhile, the cooling system and the water bath were adjusted to the setting temperature. After the preparation, the test was started by transferring the test solution into the cell using a peristaltic pump. During the test, the CO₂ was continuously purged into the test cell to avoid the oxygen contamination.

In the test using WBE, the distribution of the macro-cell current was probed every 10 min to visualize the dynamic change of TLC. Since a sudden change of the local current would occur once the measurement was performed during the droplet fallen, each current map was repeatedly measured for three times to ensure that each current mapping was performed at a steady state. Simultaneously, the endoscope was used to facilitate observing the surface status. On the basis of the current mapping and the surface observation, the cathodic sites and the anodic sites beneath or outside the water droplet could be identified. The electrodes located at both anodic sites and the cathodic sites were selected for periodically local macro-current measurement of 5 Hz. Along with the continuously local current probing, the DRT was obtained. The WCR was further evaluated according to the current mapping and DRT measurement. Meanwhile, the condensation rate was also measured through the volume calculation of the collected condensed water.

In order to further probe the local micro-cell current on WBE, some typical wire electrodes which were located in main anodic areas and cathodic areas were selected for LPR measurements. Four adjacent electrodes were selected to construct the three-electrode system (Supplementary Fig. 9). The measurement accuracy of the local three-electrode system established by same materials is verified by an additional test which is presented in Supplementary Note 10. During the LPR measurement, the selected WE was polarized from -5 mV to $+5$ mV around the open circuit potential (OCP) with an anodic scan rate of $0.5 \text{ mV}\cdot\text{s}^{-1}$. Since the solution resistance beneath the thin water film could not be neglected, the local solution resistance was measured from the electrochemical impedance using the frequency range of 10 kHz to 100 Hz with a ± 5 mV AC signal around OCP⁵². The linear polarization resistance (R_p) of the selected electrode could be calculated with the compensation of the solution resistance. After the TLC test using WBE, the surface morphology of the whole WBE was firstly observed by an EOS digital camera (Cannon, Japan) and an OLS 5000 infinite microscope (Olympus, Japan). Then, the corrosion products on the WBE were cleaned by the solution suggested in ASTM G1-03. The 3D profile of the whole WBE surface was measured by the infinite microscope. Thereafter, the corrosion depth of each wire electrode was calculated from the negative volume beneath the adjacent epoxy plane.

The test condition of the steel coupon was totally the same as the test using WBE. After 7 days of TLC test, the steel coupon was firstly taken out for surface morphology observation using both the digital camera and the infinite microscope. The corrosion products on the steel surface were further characterized using an X-ray Diffractometer (XRD, Rigku, Japan), an EM-30 Plus scanning electron microscope (SEM, Coxem, Korean) and energy dispersive spectrometry (EDS). Then, the corrosion products were cleaned and the total weight loss of the steel coupon was measured by an AUW120D analytical balance (Shimadzu, Japan) to calculate the general TLC rate.

DATA AVAILABILITY

The data that support the findings of this study are available from the corresponding author upon reasonable request

Received: 5 September 2022; Accepted: 21 February 2023;
Published online: 08 March 2023

REFERENCES

- Gunaltun, Y. M., Supriyatman, D. & Achmad, J. Top-of-line corrosion in gas lines confirmed by condensation analysis. *Oil Gas. J.* **97**, 64–72 (1999).
- Zhang, Z. et al. A mechanistic model of top-of-the-line corrosion. *Corrosion* **63**, 1051–1062 (2007).
- Singer, M. et al. CO₂ top-of-the-line corrosion in presence of acetic acid: a parametric study. *Corrosion* **69**, 719–735 (2013).
- Islam, M. M., Pojtanabuntoeng, T. & Gubner, R. Condensation corrosion of carbon steel at low to moderate surface temperature and iron carbonate precipitation kinetics. *Corros. Sci.* **111**, 139–150 (2016).
- Singer, M. Study of the localized nature of top of the line corrosion in sweet environment. *Corrosion* **73**, 1030–1055 (2017).
- Singer M. in *Trends in Oil and Gas Corrosion Research and Technologies* 689–706 (2017).
- Rozi, F. et al. Laboratory investigation on the condensation and corrosion rates of top of line corrosion in carbon steel: a case study from pipeline transporting wet gas in elevated temperature. *Corros. Eng. Sci. Technol.* **53**, 444–448 (2018).
- Hinkson, D., Zhang, Z., Singer, M. & Nescic, S. Chemical composition and corrosiveness of the condensate in top-of-the-line corrosion. *Corrosion* **66**, 0450021–0450028 (2010).
- Amri, J., Gulbrandsen, E. & Nogueira, R. P. The effect of acetic acid on the pit propagation in CO₂ corrosion of carbon steel. *Electrochem. Commun.* **10**, 200–203 (2008).
- Folena, M. C. et al. CO₂ top-of-line-corrosion; assessing the role of acetic acid on general and pitting corrosion. *Corrosion* **77**, 298–312 (2020).
- Ajayi, F. O. & Lyon, S. Mitigation of top- and bottom-of-the-line CO₂ corrosion in the presence of acetic acid (I): pH control using methyl diethanolamine. *Mater. Corros.* **72**, 1177–1188 (2021).
- Belarbi, Z. et al. Thiols as volatile corrosion inhibitors for top-of-the-line corrosion. *Corrosion* **73**, 892–899 (2017).
- Jauseau, N., Farelas, F., Singer, M. & Nešić, S. Investigation of the role of droplet transport in mitigating top of the line corrosion. *Corrosion* **74**, 873–885 (2018).
- Jevremovic, I. et al. A novel method to mitigate the top-of-the-line corrosion in wet gas pipelines by corrosion inhibitor within a foam matrix. *Corrosion* **69**, 186–192 (2013).
- Islam, M. M., Pojtanabuntoeng, T. & Gubner, R. Corrosion of carbon steel under condensing water and monoethylene glycol. *Corros. Sci.* **143**, 10–22 (2018).
- Askari, M. Development of a novel setup for in-situ electrochemical assessment of top of the line corrosion (TLC) and its smart inhibition under simulated conditions. *Process Saf. Environ. Prot.* **160**, 887–899 (2022).
- Okafor, P. C. & Nescic, S. Effect of acetic acid on CO₂ corrosion of carbon steel in vapor-water two-phase horizontal flow. *Chem. Eng. Commun.* **194**, 141–157 (2007).
- Singer, M., Camacho, A., Brown, B. & Nescic, S. Sour top-of-the-line corrosion in the presence of acetic acid. *Corrosion* **67**, 0850031–08500316 (2011).
- Singer, M., Al-Khamis, J. & Nescic, S. Experimental study of sour top-of-the-line corrosion using a novel experimental setup. *Corrosion* **69**, 624–638 (2013).
- Islam, M. M., Pojtanabuntoeng, T. & Gubner, R. Study of the top-of-the-line corrosion using a novel electrochemical probe. *Corrosion* **74**, 588–598 (2017).
- Xu, Y. Z., Huang, Y., Wang, X. N. & Lin, X. Q. Experimental study on pipeline internal corrosion based on a new kind of electrical resistance sensor. *Sens. Actuators B-Chem.* **224**, 37–47 (2016).
- Rafehi, A. Development and evaluation of thin film electrical resistance sensors for monitoring CO₂ top of the line corrosion. *Sens. Actuators B-Chem.* **346**, 130492 (2021).
- Kouril, M., Prosek, T., Scheffel, B. & Dubois, F. High sensitivity electrical resistance sensors for indoor corrosion monitoring. *Corros. Eng. Sci. Technol.* **48**, 282–287 (2013).
- Xia, D. H. et al. Electrochemical measurements used for assessment of corrosion and protection of metallic materials in the field: a critical review. *J. Mater. Sci. Technol.* **112**, 151–181 (2022).
- de Carvalho, S. S. et al. Development and evaluation of miniature electrodes for electrochemical measurements in a CO₂ top of line corrosion environment. *Corros. Eng. Sci. Technol.* **54**, 547–555 (2019).
- Islam, M. M., Pojtanabuntoeng, T., Gubner, R. & Kinsella, B. Electrochemical investigation into the dynamic mechanism of CO₂ corrosion product film formation on the carbon steel under the water-condensation condition. *Electrochim. Acta* **390**, 138880 (2021).
- Vitse, F. et al. Mechanistic model for the prediction of top-of-the-line corrosion risk. *Corrosion* **59**, 1075–1084 (2003).
- Jevremovic, I. et al. Evaluation of a novel Top-of-the-Line Corrosion (TLC) mitigation method in a large-scale flow loop. *Corrosion* **71**, 389–397 (2015).
- Xia, D. H. et al. Modeling localized corrosion propagation of metallic materials by peridynamics: progresses and challenges. *Acta Metall. Sin.* **58**, 1093–1107 (2022).
- Tan, Y. J. Wire beam electrode: a new tool for studying localised corrosion and other heterogeneous electrochemical processes. *Corros. Sci.* **41**, 229–247 (1998).
- Tan, Y. J., Bailey, S., Kinsella, B. & Lowe, A. Mapping corrosion kinetics using the wire beam electrode in conjunction with electrochemical noise resistance measurements. *J. Electrochem. Soc.* **147**, 530–539 (2000).
- Tan, Y. J., Fwu, Y. & Bhardwaj, K. Electrochemical evaluation of under-deposit corrosion and its inhibition using the wire beam electrode method. *Corros. Sci.* **53**, 1254–1261 (2011).
- Xu, Y. Z. & Tan, M. Y. Visualising the dynamic processes of flow accelerated corrosion and erosion corrosion using an electrochemically integrated electrode array. *Corros. Sci.* **139**, 438–443 (2018).
- Xu, Y. Z. & Tan, M. Y. Probing the initiation and propagation processes of flow accelerated corrosion and erosion corrosion under simulated turbulent flow conditions. *Corros. Sci.* **151**, 163–174 (2019).
- Wang, Y. et al. Study of localized corrosion of 304 stainless steel under chloride solution droplets using the wire beam electrode. *Corros. Sci.* **53**, 2963–2968 (2011).
- He, L., Xu, Y., Wang, X. & Huang, Y. Understanding the propagation of nonuniform corrosion on a steel surface covered by marine sand. *Corrosion* **75**, 1487–1501 (2019).
- Xu, Y. Z. et al. The study of the localized corrosion caused by mineral deposit using novel designed multi-electrode sensor system. *Mater. Corros.-Werkst. Und Korros.* **68**, 632–644 (2017).
- Tan, Y. J. Sensing localised corrosion by means of electrochemical noise detection and analysis. *Sens. Actuators B-Chem.* **139**, 688–698 (2009).
- Dugstad, A. Fundamental aspects of CO₂ metal loss corrosion, part I: mechanism. *Corrosion* **2015**, 534–545 (2015).
- Schmitt, G. Fundamental aspects of CO₂ metal loss corrosion. Part II: influence of different parameters on CO₂ corrosion mechanism. *Corrosion* **2015**, 546–574 (2015).
- Nescic, S. & Sun W. in *Shreir's Corrosion* (eds Cottis B. et al.) 1270–1298 (2010).
- Barker, R. et al. A review of iron carbonate (FeCO₃) formation in the oil and gas industry. *Corros. Sci.* **142**, 312–341 (2018).
- Nescic, S. Effects of multiphase flow on internal CO₂ corrosion of mild steel pipelines. *Energy Fuels* **26**, 4098–4111 (2012).
- Nordsveen, M., Nescic, S., Nyborg, R. & Stangeland, A. A mechanistic model for carbon dioxide corrosion of mild steel in the presence of protective iron carbonate films—Part 1: theory and verification. *Corrosion* **59**, 443–456 (2003).
- Zhang, G. A. & Cheng, Y. F. On the fundamentals of electrochemical corrosion of X65 steel in CO₂-containing formation water in the presence of acetic acid in petroleum production. *Corros. Sci.* **51**, 87–94 (2009).
- Sun, W. & Nescic, S. Kinetics of corrosion layer formation: part 1—iron carbonate layers in carbon dioxide corrosion. *Corrosion* **64**, 334–346 (2008).
- Zhu Y. S., et al. Understanding the influences of temperature and microstructure on localized corrosion of subsea pipeline weldment using an integrated multi-electrode array. *Ocean Eng.* **189**, 106351 (2019).
- Han J., Yang Y., Nešić S. & Brown B. J. C. Roles of passivation and galvanic effects in localized CO₂ corrosion of mild steel. *NACE* **2008**, 08332 (2008).
- Han, J., Nešić, S., Yang, Y. & Brown, B. N. Spontaneous passivation observations during scale formation on mild steel in CO₂ brines. *Electrochim. Acta* **56**, 5396–5404 (2011).
- Zhang, G. A. & Cheng, Y. F. Localized corrosion of carbon steel in a CO₂-saturated oilfield formation water. *Electrochim. Acta* **56**, 1676–1685 (2011).
- Xia, D. H. et al. Review-electrochemical noise applied in corrosion science: theoretical and mathematical models towards quantitative analysis. *J. Electrochem. Soc.* **167**, 081507 (2020).
- Hilbert, L. R. Monitoring corrosion rates and localised corrosion in low conductivity water. *Corros. Sci.* **48**, 3907–3923 (2006).

ACKNOWLEDGEMENTS

This research is sponsored by National Key R&D Program of China [No. 2022YFC2806204], Natural Science Foundation of China [No. 52001055], Fundamental Research Funds for the Central Universities [No. DUT21RC(3)093], China Postdoctoral Science Foundation [NO. 2022M722955], and The Open Foundation of State Key Laboratory of Structural Analysis for Industrial Equipment [NO. GZ22118].

AUTHOR CONTRIBUTIONS

M.W.—conceptualization, methodology, investigation, data collection, formal analysis, writing—original draft. M.Y.T.—formal analysis, writing—review and editing. Y.Z.—data collection, formal analysis. Y.H.—conceptualization, supervision, writing—review and editing. Y.X.—conceptualization, methodology, project administration, resources, funding acquisition, writing—review and editing.

COMPETING INTERESTS

The authors declare no competing interests.

ADDITIONAL INFORMATION

Supplementary information The online version contains supplementary material available at <https://doi.org/10.1038/s41529-023-00332-x>.

Correspondence and requests for materials should be addressed to Yunze Xu.

Reprints and permission information is available at <http://www.nature.com/reprints>

Publisher's note Springer Nature remains neutral with regard to jurisdictional claims in published maps and institutional affiliations.



Open Access This article is licensed under a Creative Commons Attribution 4.0 International License, which permits use, sharing, adaptation, distribution and reproduction in any medium or format, as long as you give appropriate credit to the original author(s) and the source, provide a link to the Creative Commons license, and indicate if changes were made. The images or other third party material in this article are included in the article's Creative Commons license, unless indicated otherwise in a credit line to the material. If material is not included in the article's Creative Commons license and your intended use is not permitted by statutory regulation or exceeds the permitted use, you will need to obtain permission directly from the copyright holder. To view a copy of this license, visit <http://creativecommons.org/licenses/by/4.0/>.

© The Author(s) 2023